

Supplementary file for: Seasonal icings reveal subsurface water drainage of a Greenland Ice Sheet outlet glacier

Rebecca McCerery¹, Joseph A. Graly¹, Christopher L. Hansen², Kate Winter¹, William P. Gilhooly III³, Trinity L. Hamilton^{2,4}, Moses Jatta³, Jeff R. Havig², Felipe Napoleoni^{1,5}, Alicia M. Rutledge⁶, Matthew Terrell³, Tanya M. Trott⁷, Kayla Woodie³, Bernd Kulesa⁷, Sevi Modestou¹, Hannah Bahrani¹, Tori Kennedy⁸, Alexandra Messerli⁹, Kathy Licht³

¹*School of Geography and Natural Sciences, Northumbria University, Newcastle-upon-Tyne, United Kingdom, NE1 8ST*

*Corresponding author rebecca.mccerery@hotmail.com

¹School of Geography and Natural Sciences, Northumbria University, Newcastle Upon Tyne, NE1 8ST, United Kingdom

²Department of Plant and Microbial Biology, University of Minnesota, Saint Paul, MN 55108

³Department of Earth & Environmental Sciences, Indiana University Indianapolis, Indianapolis, IN 46202 USA

⁴The BioTechnology Institute, University of Minnesota, Saint Paul, MN 55108

⁵School of Geosciences, University of Edinburgh, Edinburgh, EH8 9XP, United Kingdom

⁶Department of Astronomy and Planetary Science, Northern Arizona University, Flagstaff, AZ 86011 USA

⁷School of Biosciences, Geography and Physics, Swansea University, Swansea, SA2 8PP, United Kingdom

⁸Earth and Environmental Sciences, Indiana University Indianapolis, Indianapolis, United States

⁹Asiaq Greenland Survey: Nuuk, GL

S1 Naled and Accreted Ice Core Photographs



Figure S1 (a) and (b) naled core I1; (c) and (d) naled core I2; (e) and (f) naled core I3; (g) naled core I4; (h) naled core I5.



Figure S2 (a) naled core I6; (b) naled core I7; (c) naled core I8; (d) naled core I9; (e) and (f) naled core I10; (g) naled core I11; (h) naled core I12.



Figure S3 (a) accreted core A1; (b) accreted core A2; (c) accreted core A3; (d) accreted core A4

S2 Time Lapse Camera Information

Table S1 Time lapse camera recording dates and locations.

Season	Camera Number	Lat (N)	Long (W)	Orientation	Dates Active	Camera Placement	Observations
Winter 22-23	1	67.18100	-50.33421	S	12/09/22-21/09/22	View of the main meltwater channel towards the hillslopes.	River freezing but no naled or accreted ice formations.
	2	67.18107	-50.33498	S	12/09/22-11/03/23	View of the main meltwater channel towards the hillslopes.	River freezing but no naled or accreted ice formations.
	3	67.18093	-50.33572	SE	12/09/22-12/03/23	View east towards the glacier across the main meltwater channel overlooking areas of accreted ice formation.	Ice development on the main channel and ice cored sediment wastage in the forefront.
	4	67.18066	-50.33645	SW	13/10/22-18/10/22	View west up the smaller lateral meltwater channel towards the glacier front.	Camera fell down after 4 days of recording.
	5	67.18080	-50.33721	S	13/10/22-04/03/23	View southeast of large sediment terrace overlooking the main meltwater channel.	Stable accreted ice lasting the full filming period with episodes of wastage and building (likely from snow input).
	6	67.18143	-50.33553	S	15/10/22-28/10/22	View southwest towards the moraines and over an arm of the main meltwater channel.	Captured accreted ice wastage before camera collapse.
Winter 23-24	1	67.18091	-50.34077	E	19/09/23-08/10/23	View from west of forefield down the main meltwater channel.	Large subglacial outburst from 28/09 to 5/10 peaking on 01/10. Camera captures the site of the eruption and the increased flow downstream of the main meltwater channel.
	2	67.18165	-50.33546	W	20/09/23-30/11/23	View from moraine overlooking previously identified proglacial upwellings.	Camera has full view of a proglacial upwelling. Part of the outburst flow fully captured in camera 1 is seen in the foreground. A naled forms at the site of the upwelling in mid-October with full view of the formation until November when

							the camera fails.
	3	67.18047	-50.33504	S	21/09/23-30/11/23	View of a previously identified large proglacial upwelling.	River level rise and fall with subglacial water drainage and large outflow events.
	4	67.18064	-50.33528	W	21/09/23-03/04/24	View of previously identified proglacial upwelling.	Large outflow and proglacial upwelling eruption in September-October 2023 captured.
	5	67.17775	-50.34442	NE	21/09/23-06/22/23	Placement on the south marginal stream.	Observed changes in river discharge.
	6	67.17664	-50.33838	NW	21/09/23-03/04/24	View overlooking previously identified proglacial upwelling with orange coloured waters.	Outflow of orange-yellow coloured waters and the formation of smaller naledi was captured in October 2023, coinciding with large proglacial eruption closer to the glacier ice margin.

S3 Electrical Resistivity Tomography Methods

All data were processed and inverted using ResIPy v3.6.3 (Blanchy et al., 2020). Initial inspection of the SuperSting file format using ResIPy revealed highly inconsistent reciprocal misfits and non-physical patterns across pseudosections, indicating that reciprocal measurements were not correctly recorded (Koestel et al., 2008; Mwakanyamale et al., 2012). As a result, standard reciprocal error filtering was deemed inappropriate for this dataset. In the absence of reciprocal measurements, a manual quality control workflow was applied. This included the removal of outliers from pseudosections (e.g., extreme spikes, low signal-to-noise values, and measurements associated with poor electrode contacts), consistent with established approaches (Binley, 2015). A two-term error model was implemented using an absolute error weight (a_wgt) of 0.001 and a proportional error weight (b_wgt) of 0.02, as recommended for datasets lacking reciprocal-based error calibration (Binley & Kemna, 2005; Blanchy et al., 2020).

Triangular meshes are commonly recommended for modeling topographically complex or geologically heterogeneous environments such as Arctic and sub-Arctic glacier forelands (Rücker et al., 2017). A triangular finite-element mesh was generated for this dataset in ResIPy using Gmsh (Geuzaine & Remacle, 2009). The mesh design balanced computational efficiency with the resolution needed to capture shallow structures across the permafrost–active layer transition. A fine/coarse boundary depth of 30 m was used, and seven elements were placed between electrodes with a vertical growth factor of 1.1 (Oldenburg & Li, 1999). This configuration ensured sufficient detail to resolve metre-scale variations in resistivity across the top ~10–15 m of ground (Mewes et al., 2017).

The inversion was conducted in a logarithmic data space using a regularised solution with linear filtering, known for its robustness in high-contrast geological settings (Binley & Kemna, 2005). The inversion was run for up to 20 iterations, with a normal regularisation mode used in the absence of a reference or time-lapse model. This resulted in stable resistivity models for both profiles, revealing coherent structures indicative of thawed surface layers and deeper frozen sediments. Consistent meshing and inversion settings enabled visualisation and structural interpretation across intersecting lines.

To enhance boundary detection, the vertical gradient of resistivity (GradRho_z) was calculated for both profiles. Gradient-based methods are widely used to highlight sharp resistivity contrasts, such as the transition between thawed and frozen ground (Hauck & Kneisel, 2008; Thompson et al., 2017; Mewes et al., 2017). The volumetric resistivity field was exported to ParaView, where the gradient field ($\nabla\rho$) was computed using built-in derivative tools. The vertical component ($\partial\rho/\partial z$) was then extracted to isolate depth-dependent changes in resistivity.

Sharp positive vertical gradients ($\partial\rho/\partial z > 0$) were interpreted as the base of the active layer, marking the onset of ice-rich permafrost, while negative gradients ($\partial\rho/\partial z < 0$) suggested zones of thaw or saturation. Compared to raw resistivity values, vertical gradients provided more precise indicators of subsurface boundary locations and enhanced the lateral continuity of interpreted features (Hauck & Kneisel, 2008).

Binley, A.: Tools and techniques: Electrical methods. *Treatise on geophysics*, 233-259, 10.1016/b978-0-444-53802-4.00192-5, 2015.

Binley, A. and Kemna, A.: DC resistivity and induced polarization methods. In *Hydrogeophysics*, Dordrecht: Springer Netherlands, 129-156, 2005.

Blanchy, G., Saneiyani, S., Boyd, J., McLachlan, P., and Binley, A.: ResIPy, an intuitive open source software for complex geoelectrical inversion/modeling, *Computers & Geosciences*, 137, 104423, 10.1016/j.cageo.2020.104423, 2020.

Geuzaine, C. and Remacle, J.F.: Gmsh: A 3-D finite element mesh generator with built-in pre-and post-processing facilities. *International journal for numerical methods in engineering*, 79(11), 1309-1331, 10.1002/nme.2579, 2009

Hauck, C. and Kneisel, C.: *Applied geophysics in periglacial environments (Vol. 10)*. Cambridge University Press, 2008.

Koestel, J., Kemna, A., Javaux, M., Binley, A. and Vereecken, H.: Quantitative imaging of solute transport in an unsaturated and undisturbed soil monolith with 3-D ERT and TDR. *Water resources research*, 44(12), 10.1029/2007WR006755, 2008

Mewes, B., Hilbich, C., Delaloye, R. and Hauck, C.: Resolution capacity of geophysical monitoring regarding permafrost degradation induced by hydrological processes. *The Cryosphere*, 11(6), 2957-2974, 10.5194/tc-11-2957-2017, 2017.

Mwakanyamale, K., Slater, L., Binley, A. and Ntarlagiannis, D.: Lithologic imaging using complex conductivity: Lessons learned from the Hanford 300 Area. *Geophysics*, 77, 397–E409, 10.1190/geo2011-0407.1, 2012.

Oldenburg, D.W. and Li, Y.: Estimating depth of investigation in dc resistivity and IP surveys. *Geophysics*, 64(2), 403-416, 10.1190/1.1444545, 1999.

Rücker, C., Günther, T. and Wagner, F.M.: pyGIMLi: An open-source library for modelling and inversion in geophysics. *Computers & Geosciences*, 109, 106-123, 10.1016/j.cageo.2017.07.011, 2017.

Thompson, S.S., Kulesa, B., Benn, D.I. and Mertes, J.R.: Anatomy of terminal moraine segments and implied lake stability on Ngozumpa Glacier, Nepal, from electrical resistivity tomography (ERT). *Scientific Reports*, 7(1), 46766, 10.1038/srep46766, 2017

S4 Stable water isotope standard measurements

Table S2. Summary of water isotope measurement monitor standards (post normalization). All values in per mille VSMOW-SLAP. Note that the first VSMOW2 $\delta^2\text{H}$ value is omitted, due to a particularly strong memory effect on that measurement. Results of drift standards from the same run (19/03/2025) do not show significant variance or offsets, reinforcing this assessment.

Standard	Vial #	$\delta^2\text{H}$ +/- SE	$\delta^{18}\text{O}$ +/- SE	Run start date
VSMOW2	6		-0.26± 0.05	19/03/2025
VSMOW2	6	-0.7± 0.3	0.46± 0.05	26/03/2025
VSMOW2	11	-0.7± 0.4	0.31± 0.05	03/04/2025
VSMOW2	7	0.6± 0.3	0.60± 0.05	10/04/2025
	SD	0.75	0.38	
Medium Natural Water	1	-98.9± 0.3	-12.57± 0.05	19/03/2025
Medium Natural Water	7	-99.8± 0.3	-12.64± 0.05	19/03/2025
Medium Natural Water	24	-98.1± 0.3	-12.55± 0.05	19/03/2025
Medium Natural Water	40	-98.4± 0.3	-12.61± 0.05	19/03/2025
Medium Natural Water	56	-98.2± 0.3	-12.24± 0.05	19/03/2025
Medium Natural Water	75	-99.7± 0.3	-12.78± 0.05	19/03/2025
	SD	0.75	0.18	
Medium Natural Water	1	-99.0± 0.3	-12.54± 0.05	26/03/2025
Medium Natural Water	22	-99.5± 0.3	-12.64± 0.05	26/03/2025
Medium Natural Water	38	-99.0± 0.3	-12.46± 0.05	26/03/2025
Medium Natural Water	54	-99.1± 0.3	-12.54± 0.05	26/03/2025
Medium Natural Water	74	-99.1± 0.3	-12.58± 0.05	26/03/2025
	SD	0.21	0.07	
Medium Natural Water	1	-99.1± 0.3	-12.39± 0.06	03/04/2025
Medium Natural Water	10	-101.2± 0.3	-12.78± 0.06	03/04/2025
Medium Natural Water	42	-99.4± 0.3	-12.49± 0.06	03/04/2025
Medium Natural Water	58	-99.0± 0.3	-12.34± 0.06	03/04/2025
	SD	1.03	0.2	
Greenland Water	1	-114.4± 0.3	-16.09± 0.05	10/04/2025
Greenland Water	6	-115.1± 0.3	-16.16± 0.05	10/04/2025
	SD	0.49	0.05	

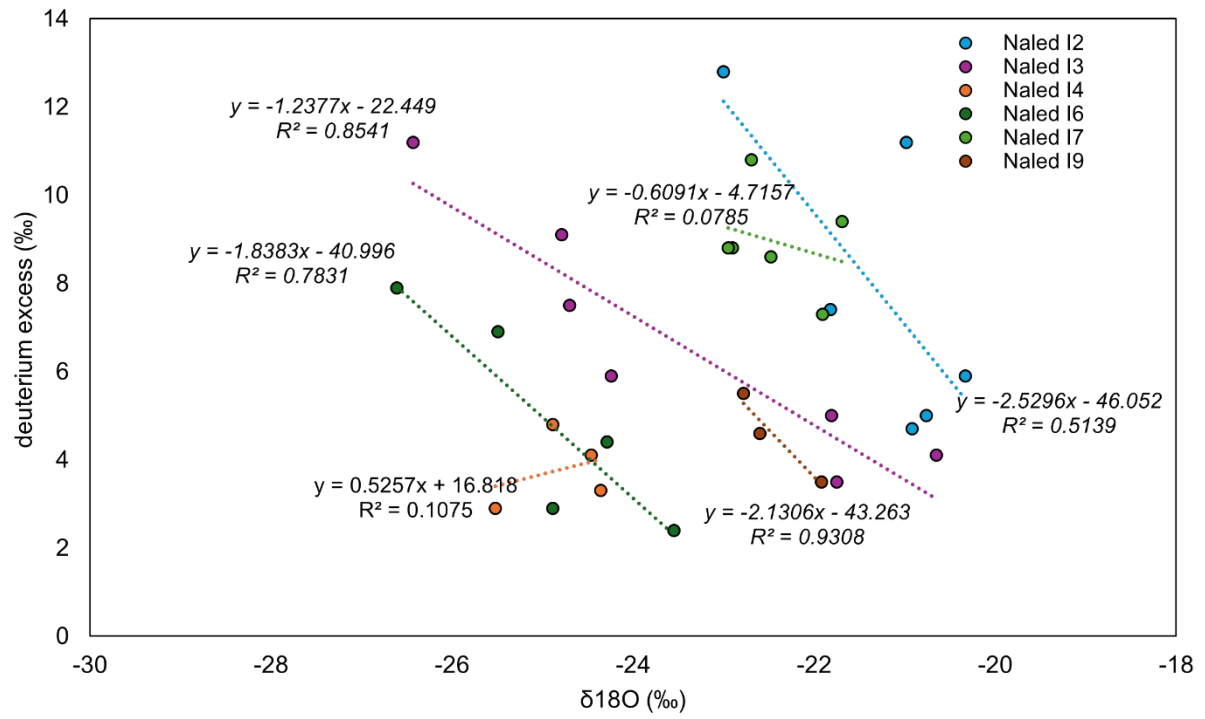


Figure S4 Cross-plot of deuterium excess vs $\delta^{18}O$ of naled ice samples.